Check for updates

CuBi$_2$O$_4$ photocathode with integrated electric field for enhanced H$_2$O$_2$ production

Mengdi Sun [a,b], Bo Liu [a], Weihua Han [a], Zemin Zhang [a,*], Mingzheng Xie [b,*]

[a] *School of Physical Science and Technology, Lanzhou University, Lanzhou 730000, China*
[b] *Key Laboratory for Environmental Pollution Prediction and Control of Gansu Province, College of Earth and Environmental Sciences, Lanzhou University, Lanzhou 730000, China*

A R T I C L E   I N F O

A B S T R A C T

Metal oxide semiconductors are promising for photosynthetic H$_2$O$_2$ production, provided the issue of excessive charge recombination can be adequately addressed. Inducing internal electric field is a common remedial strategy to inhibit carrier recombination but challenging to accomplish without external power input. To overcome this drawback, a novel photocathode was designed and fabricated by combing photothermoelectricity and photoelectricity by adding a NaCo$_2$O$_4$ film under the CuBi$_2$O$_4$ film to generate an internal electric field from photoinduced temperature gradients. Our results show the significantly enhanced photoelectrochemical activity for the composite photocathode with an H$_2$O$_2$ production concentration of 192.9 μmol/L, 2.4 times higher than CuBi$_2$O$_4$. Photocurrent under controlled temperature gradients and COMSOL simulation defined that the enhancement comes from the synergy of photothermoelectricity and photoelectricity. This work demonstrates a feasible strategy to inhibit carrier recombination in photoelectrode with internal thermoelectric potential, which can significantly enhance the energy conversion efficiency without extra energy consumption.

1. Introduction

Hydrogen peroxide (H$_2$O$_2$), an eco-friendly oxidant and potential energy carrier, have been widely applied in the chemical industry, medical disinfection, and environmental protection efforts [1–4]. However, so far, the well-established anthraquinone oxidation process involves many drawbacks, including the safety issue for transportation, the need for H$_2$, noble metal catalysts, organic sacrificial agents, etc. Therefore, an environmentally friendly alternative is highly desired for economic and benign H$_2$O$_2$ formation [5]. Recently, photo-electrochemical (PEC) methods have been reported as promising approaches to produce green H$_2$O$_2$. Typically, photogenerated electrons and holes in photoelectrodes are used to reduce oxygen or oxidize water, producing H$_2$O$_2$ at the photocathode or photoanode, respectively [6,7]. Developing a high-efficiency and low-cost photoelectrode for H$_2$O$_2$ production has been an important yet elusive goal. To date, metal oxide semiconductors have shown the most promise as candidate photoelectrode materials due to suitable bandgaps, stability, and ease of fabrication [8,9]. However, despite much development effort, practical performance is still not up to our ideal requirements.

Balancing the generation and collection of charge carriers is challenging for most metal oxide semiconductors because of relatively low carrier mobilities and short carrier diffusion lengths arising from small polaron hopping conduction mechanisms [10–12]. As reported by Sharp et al. [13] for Cu$_3$V$_2$O$_8$ photoanodes, most charge carriers are collected within 10 nm of the electrode surface, with approximately 98% of photogenerated charge carriers lost to bulk recombination. Therefore, developing new strategies to inhibit bulk carrier recombination is a critical task on the way to successfully realizing the future solar-to-H$_2$O$_2$ economy.

The two most common strategies for overcoming surface-related charge carrier recombination are surface passivation and heterostructure construction, which fail to effectively inhibit carrier recombination in bulk [14,15]. Yet, for a solid-solid or solid-liquid junction, most charge recombination occurs in the bulk and the field-free region due to the absence of a driving force [16]. In the space charge region, electrons and holes will effectively achieve spatial separation under the driving force from the internal electric field. The electric field is the driving force for the directed migration of charges, so internal electric field inducement is the most promising approach to inhibit charge recombination in bulk [17–19]. Recently, integrating multi-physical properties (e.g., thermoelectricity, piezoelectricity, or ferroelectricity)

---

* Corresponding authors.
E-mail addresses: zhangzemin@lzu.edu.cn (Z. Zhang), xiemzh@lzu.edu.cn (M. Xie).

into PEC devices to generate internal electric fields has been considered a significant advancement in PEC [20–22]. Given that the photothermal phenomenon always occurs along with the photovoltaic effect converting "waste heat" to use electricity to drive the separation and transport of charge carriers in the bulk of photoelectrodes is a favored approach to improve the efficiency of PEC systems [23,24].

In this work, the p-type semiconductor $CuBi_2O_4$ (denoted as CBO) [25–27] was chosen as a prototypical photoelectrode material and combined with $NaCo_2O_4$ (denoted as NCO), one of the best thermoelectric materials [23], to fabricate a novel composite photocathode (NCO/CBO). Upon illumination, the composite film exhibited a strong photothermal effect with a maximum temperature gradient of around 29 °C. Due to the high Seebeck coefficient of NCO (150–200 uV K^{-1}), an electric field was produced within the photoexcited films. As a result, the NCO/CBO photoelectrode showed a photocurrent enhancement to − 2.38 mA cm^{-2} (+ 64%) as well as an extended carrier lifetime (+ 11%) during one-sun illumination. Temperature gradient-dependent performance indicates the synergistic effect of photothermoelectricity and photoelectricity, which was confirmed with COMSOL simulation: the NCO thermoelectric material converts temperature gradient to electricity which drives the separation and transport of photogenerated charge carriers in the bulk of the CBO film. Finally, the optimized photoelectrode exhibits relatively high H_2O_2 production. This work demonstrates a novel photothermoelectric approach for creating an electric field within the bulk of semiconductors, combining the advantages of the photothermal effect and thermoelectricity to improve photoelectricity. The strategy demonstrated here is not unique to PEC systems for H_2O_2 production and may be used to benefit all photoelectronic devices.

2. Experimental section

All chemical reagents used in this work were purchased from Sigma-Aldrich and used without further treatment.

2.1. Synthesis of NaCo₂O₄ powders by hydrothermal method

The primary $NaCo_2O_4$ powder synthesis process by the hydrothermal method is as follows: First, 15 mol/L NaOH solution was prepared using deionized water and kept stirring until the solution cooled to room temperature. Then 15 mM $Co(OH)_2$ was dissolved in the above solution with magnetic stirring for 30 min to achieve a uniform blue solution. Second, a certain amount of H_2O_2 solution (GR, 30 wt% in H_2O) was added to the above mixture dropwise under continuous stirring. The volume ratio of added H_2O_2 in the total mixed solution is about 10%. The H_2O_2 addition will result in the generation of gas bubbles and the change of solution color to yellowish-brown. Third, the above solution was transferred into a Teflon-lined stainless-steel autoclave with 80% filling degree and kept under 220 °C for 16 h, with a ramp rate of 2 °C/min. After cooling down, the black powder was collected, washed with deionized water repeatedly, and dried in an oven at 60 °C for several hours.

2.2. Preparation of NCO, CBO, and NCO/CBO films

FTO glass substrate was thoroughly cleaned with a glassware cleaning agent, anhydrous ethanol, and deionized water, followed by plasma cleaning after drying with a nitrogen gun. To obtain a uniform NCO suspension, 0.02 g of fully ground NCO powders and 0.02 g of polyethylene pyrrolidine were added to 3 g of isopropanol solution, followed by stirring. The CBO solution was prepared by adding 0.5 mM $Cu(NO_3)_2$ and 1.0 mM $Bi(NO_3)_3$ into an ethylene glycol methyl ether solution successively, and the mixture was immediately followed by sonicating and magnetic stirring to obtain a clear and transparent blue solution.

Next, thin-film samples were prepared by spin coating. The specific

spin coating steps are as follows: First, a slow-speed spin coating process was carried out. The precursor (NCO or CBO solution) was quickly and evenly spread over the surface of clean FTO secured by vacuum. Spin coating was performed at 100 rpm for 200 s. A heating lamp was located about 10 cm above the FTO substrate to accelerate solution evaporation during the spin coating process. The films were then transferred to a heating plate at 350 °C to pyrolyze for 10 min. Second, two high-speed spin coating processes were performed. The overall process was similar to the first but performed at 1000 rpm for 30 s without the aid of the heating lamp. Bare NCO and CBO thin films were prepared in this manner. For the NCO/CBO sample, the lower and upper layers were NCO and CBO, respectively. After the spin coating, all samples were annealed at 500 °C for 1 h with a ramp of 5 °C/min.

2.3. Characterization of NCO, CBO, and NCO/CBO films

The crystalline structure of the film samples was investigated by Grazing incident X-ray diffraction (XRD, Philips X′pert pro, Cu Kα, 0.15406 nm) patterns. The incident angle was 1°. Raman spectra were recorded using a confocal Raman microscope (LabRam HR, Horiba Jobin Yvon) with a 532 nm laser source. The surface composition was studied based on the X-ray photoelectron spectra (XPS, Kratos-AXIS ULTRA DLD). The microcosmic morphologies of the prepared samples were characterized by a scanning electron microscope (SEM, FEI Apreo S). Optical absorption spectra of the film samples between 300 nm and 1100 nm were also recorded using a spectrophotometer (TU-1901). SPV was used to investigate the photoelectric properties of the photoanodes as the processes of charge separation and transport at the photoanode interface can be obtained.

2.4. PEC characterization

PEC measurements (PEC, RST5200 Zhenzhou Shiruisi Instrument Technology Co., China) were performed in a special homemade electrolytic cell using a standard three-electrode system to obtain the photovoltage current response of photocathodes under AM 1.5 light illumination. The prepared photocathodes were used as the working electrodes, Ag/AgCl served as the reference electrode, and a platinum foil was used as the counter electrode. The electrolyte was 0.1 M potassium bicarbonate (Sigma Aldrich, ≥ 99.95%) with 0.1 M sodium persulfate (Sigma Aldrich, Reagent, ≥ 98%) as the electron scavenger at pH 8.2. Simulated AM 1.5 G solar illumination was provided by a high-voltage Xe lamp (500 W) with a light intensity of 100 mW cm^{-2}. Linear sweep voltammetry (LSV) was used to scan in the range of 0.5 to − 0.3 V (vs. Ag/AgCl) at a scanning rate of − 10 mV/s. IPCE was measured under a constant potential (0.5 V vs. Ag/AgCl).

2.5. PEC synthesis of H₂O₂

A homemade two-chamber cell was utilized in PEC ORR for the production of H_2O_2. The working electrode (CBO, NCO/CBO photocathode) and the counter electrode (Pt) were separated by a Nafion membrane to prevent the re-oxidation of H_2O_2 to O_2. Ag/AgCl was used as a reference electrode located near the working electrode. The mixed phosphate aqueous solution (pH 6.86) was added into the two chambers as an electrolyte, and the constant temperature was maintained through semiconductor refrigeration and water circulation. The PEC ORR was implemented by bubbling O_2 for 30 min with continued O_2 flow throughout the experiment. A 500 W Xe-lamp (AM 1.5G, 100 mW cm^{-2}) was chosen as the light source, with a distance of 15 cm from the reaction solution. Photocurrent-time (I-t) curves were obtained by applying an applied bias voltage of 0.4 V vs. RHE to the working electrode. During the reaction, 2 mL of solution was taken from the reactor every 10 min. The amount of H_2O_2 produced was determined by the iodometric method [28]. 1 mL 0.1 M potassium acid phthalate ($C_8H_5KO_4$) and 1 mL 0.4 M potassium iodide (KI) aqueous solution were

simultaneously added to 2 mL reaction solution and stirred vigorously for 2 min. Then, the absorbance at 351 nm was measured by an ultraviolet-visible spectrophotometer (TU-1901).

2.6. Numerical simulation

The thermoelectric property of NCO and its influence on the potential and carrier distribution of CBO were studied using COMSOL Multiphysics software (version 5.6). The hill-shaped part stands for NCO, and its upper layer stands for CBO. In the module of "Heat Transfer in Solids," the temperature of the bottom of NCO was set to 348.35 K or 298.15 K, and the top was 298.15 K. In the module of "Electric Currents," the bottom boundary of NCO was grounded. In the module of "Semiconductor," the acceptor concentration (p-type) in CBO was set to $1 \times 10^{15}/cm^3$. The thermoelectric potential generated by NCO was applied to the CBO layer equivalently.

3. Results and discussion

3.1. Structure and Morphology

The NCO, bare CBO, and composite NCO/CBO films were prepared using a spin coating. Fig. 1a illustrates the fabrication process for the NCO/CBO photocathodes. NCO films were spin-coated on FTO substrates using freshly synthesized NCO nanosheets as the precursor. Then, CBO overlayers were deposited on the surface of NCO by an additional spin-coating process. The resultant films were further annealed in an ambient atmosphere to obtain the final composite samples, as displayed in Fig. 1b.

The crystal structure and chemical composition of the films were investigated by X-ray diffraction (XRD) and Raman analysis. The sharp high-intensity diffraction peaks of NCO and bare CBO films in Fig. 1c are well-matched to $NaCo_2O_4$ (JCPDS No.73-0133) and $CuBi_2O_4$ (JCPDS No. 42-0334) [29–31] with good crystallinity. For the composite film, all peaks are well-matched to bare CBO, indicating that the bottom NCO layer does not have a noticeable effect on the crystal structure of the top CBO layer. The Raman spectra in Fig. 1d are indicative of NCO and CBO [32,33]. The characteristic peaks in the composite film are consistent
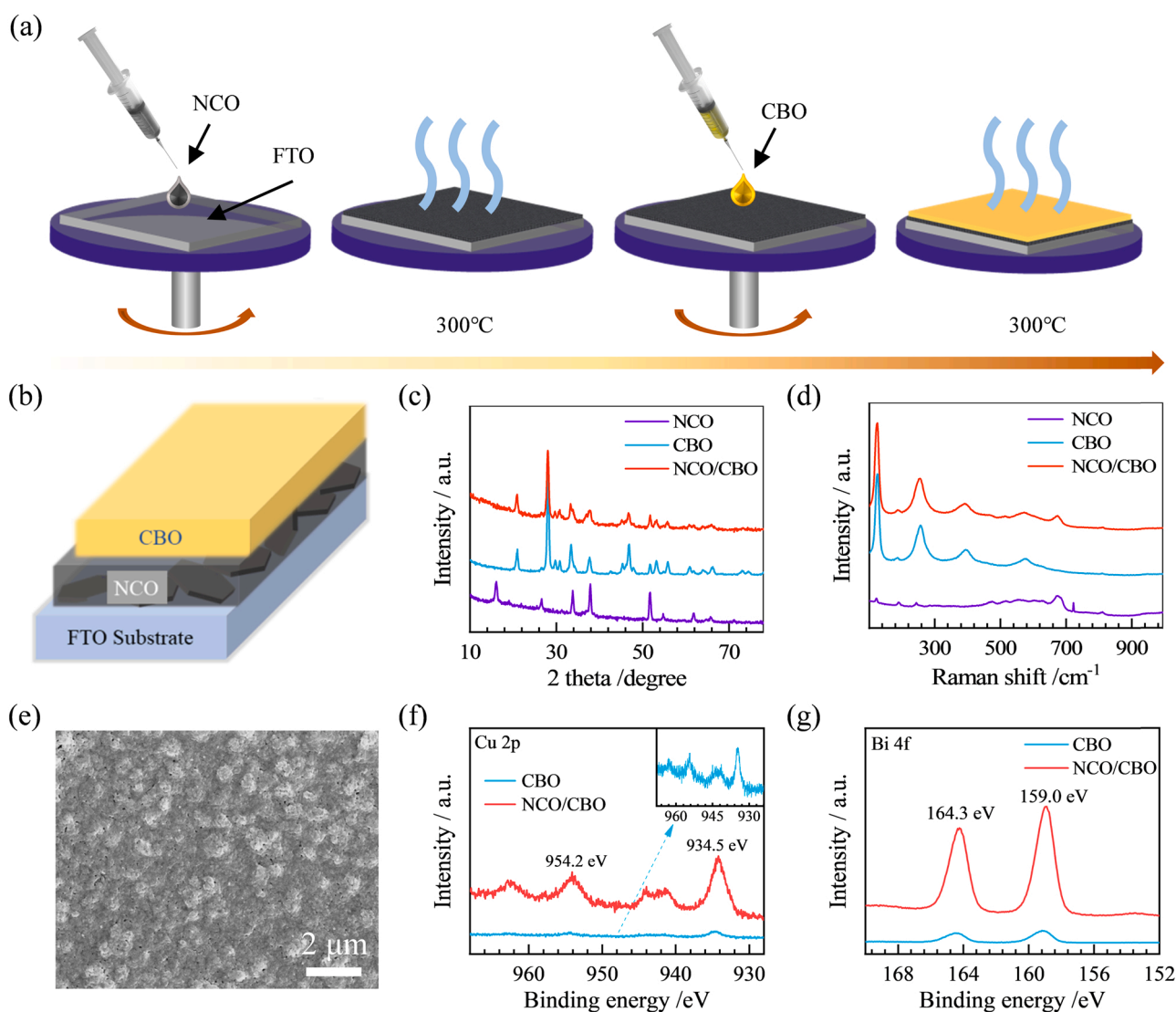

Fig. 1. Schematic illustration of the fabrication procedure for NCO/CBO composite films (a). Structure diagram of the NCO/CBO composite sample (b). The XRD (c) and Raman (d) spectra of NCO, CBO, and NCO/CBO films. Top-view SEM image of NCO/CBO film (e). High-resolution XPS spectra of Cu 2p (f) and Bi 4f (g) of CBO and NCO/CBO films.

with both CBO and NCO, indicating successful preparation of the intended NCO/CBO composite.

The microstructure and element composition of the films were studied using a scanning electron microscope (SEM) and energy-dispersive X-ray (EDX) spectra. Figs. S2–5 shows that the NCO nanosheets have a diameter of 200–500 nm and are evenly distributed on the FTO substrate, while CBO film exists as a much more compact and homogenous layer. For the NCO/CBO composite film, the NCO nanosheets are tightly wrapped by a continuous CBO layer, as illustrated in the top-view SEM images (Fig. 1e) and cross-section EDX maps (Fig. S4, Fig. S5e, f).

X-ray photoelectron spectroscopy (XPS) measurements were carried out to investigate the surface chemical compositions of the prepared films. The survey spectrum of NCO/CBO in Fig. 1f, g, and Fig. S7, 8 indicate the existence of Cu, Bi, Na, and Co atoms. The core-level spectra of Cu 2p and Bi 4f with splitting energy of 19.7 eV and 5.3 eV correspond to the reported values for Cu^{2+} and Bi^{3+} [34]. The similar core-level spectra of CBO and NCO/CBO film (Fig. 1f,g) indicate the inducement of NCO does not change the chemical environment.

3.2. PEC performance evaluation and synthesis of H_2O_2

The result of the integrated photothermoelectric effect on PEC performance was evaluated in a standard PEC system. Three films were assembled as photoelectrodes (NCO, CBO, and NCO/CBO), and the current-voltage (J-V) response was measured under long-time one-sun illumination. The long-time illumination was expected to allow for heat accumulation and thus observation of possible thermoelectric conversion. To avoid any contributions from electrolyte heating, a chilling system with a semiconductor cooling plate and peristaltic pump circulation was employed to maintain the electrolyte at a constant temperature (5 °C). The J-V curves were collected every 5 min for a total of 60 min as the light switched on and off.

The J-V curves are shown in Fig. 2, with dashed lines representing dark current. For the bare NCO sample, Fig. 2a, the current increased only slightly within the first 10 min of illumination, with a negligible

additional increase throughout the 35 min exposure. For the bare CBO sample, Fig. 2b, the photocurrent greatly increased upon initial illumination over the first 5 min, after which time it remained relatively constant. For the NCO/CBO composite, Fig. 2c, the current immediately increased upon illumination and steadily increased over the 35 min exposure. Fig. S9 displays the photocurrent as a function of time at 0.45 V vs. RHE for all three photoelectrodes to better quantify photocurrent enhancement. During light illumination, the NCO photoelectrode increased from − 0.1 to − 0.14 mA cm^{-2} (a 40% enhancement), while the bare CBO photoelectrode remained constant at − 1.15 mA cm^{-2} (a 0% enhancement). The photocurrent of NCO/CBO rapidly increased from − 1.57 mA cm^{-2} to − 2.38 mA cm^{-2} (a 64% enhancement). It is important to note the difference in current change during light on and off moments. When the light is turned on, the photocurrent of bare NCO and NCO/CBO photoelectrodes increases gradually, while that of bare CBO immediately shows a significant increase in photocurrent. When the light was turned off, the current for both NCO and NCO/CBO decreased gradually, while that of CBO decreased immediately. These results indicate that CBO exhibits a strong photoelectric property, while NCO shows evident photothermoelectric property. Therefore, the excellent performance of the NCO/CBO composite photoelectrode may potentially be attributed to a synergistic effect between the photoelectricity of CBO and the photothermoelectricity of NCO.

To evaluate PEC synthetic activities of CBO and NCO/CBO, H_2O_2 production experiments were carried out in a homemade two-chamber cell, as shown in Fig. 2d. In the ORR process, O_2 and H_2O can be reduced to H_2O_2 by a two-electron pathway [35]. Fig. 2e shows the production of H_2O_2 as a function of time under AM 1.5 irradiation under an applied bias at 0.4 V vs. RHE. The H_2O_2 concentration of NCO/CBO was 192.9 μmol/L, about 2.4 times higher than CBO, revealing that the combination of NCO with CBO could dramatically accelerate H_2O_2 formation.

The faradaic efficiency (FE) [36] for H_2O_2 production was determined based on the typical calculation, as shown in Eq. (3):
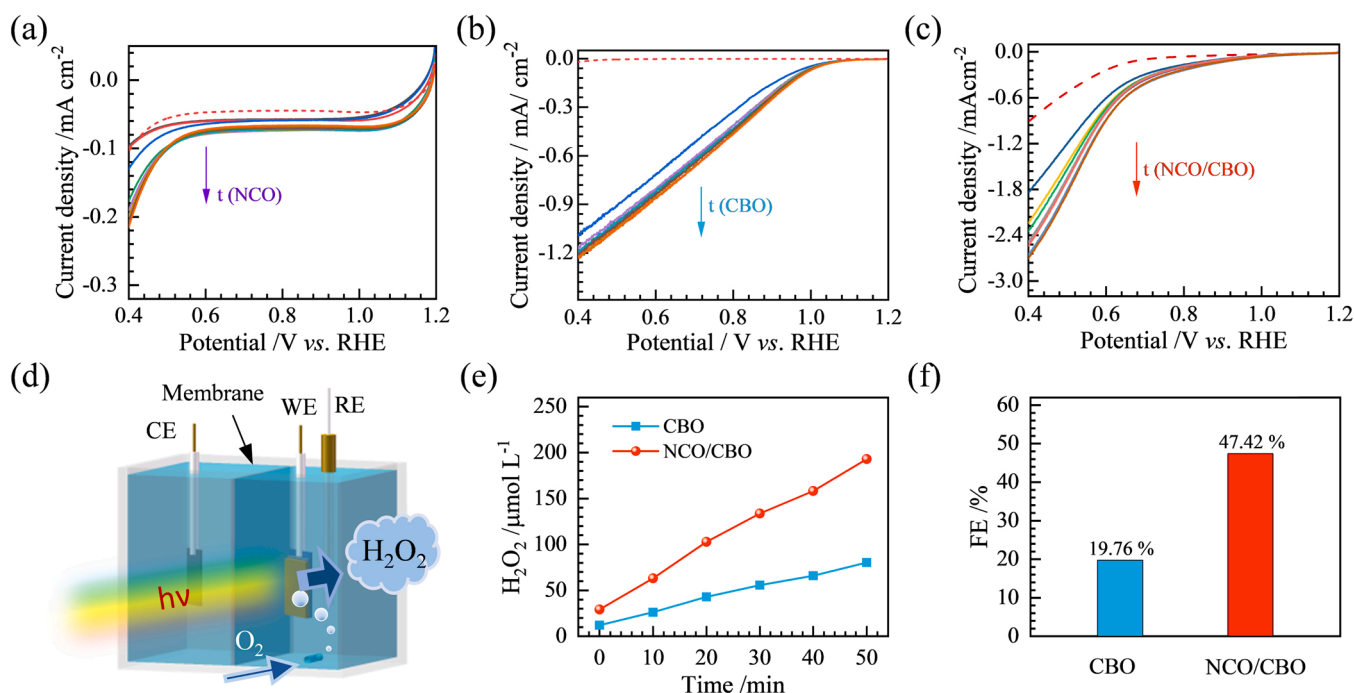

Fig. 2. The J-V curves of NCO (a), CBO (b), NCO/CBO (c) under long time one-sun illumination in 0.1 M KHCO$_3$ with 0.1 M Na$_2$S$_2$O$_8$ (pH 8.2) as the electron scavenger. The dotted lines represent the dark currents. Schematic illustration of PEC system for photocathode production of H_2O_2 through the ORR (d). PEC activities (e) and FE (f) of CBO and NCO/CBO for H_2O_2 production in mixed phosphate aqueous solution (pH 6.86).

$$FE \quad (\%) = \frac{2 \times \quad N(H_2O_2) \quad \times \quad 96485}{Q} \times 100\% \tag{3}$$

Where $N(H_2O_2)$ represents the amount of H_2O_2 produced, and Q refers to the total charge generated. Fig. 2f illustrates the FE of oxygen reduction using CBO or NCO/CBO. The NCO/CBO composite achieved a favorable FE of 47.42%, while CBO was only 19.76%. The enhancement is following the results of PEC performance, which indicates the positive effect of the synergy of the photoelectricity of CBO and the photo-thermoelectricity of NCO.

3.3. Synergy of photothermoelectricity and photoelectricity

The light-harvesting capacity of the films was evaluated from UV–vis–NIR light absorption spectra provided in Fig. 3a [37]. The NCO film with black color shows strong light absorption over the entire wavelength range (300–1100 nm). The CBO film shows absorption at wavelengths below 700 nm, consistent with its optical bandgap (1.6 eV, Fig. S10) [38]. The NCO/CBO composite film shows an absorption spectrum resembling that of NCO, indicating that the NCO layer can effectively harvest visible NIR photons. Generally, in semiconductors, absorbed NIR photons generate phonons and produce heat (rather than free carriers). Due to heat accumulation, a temperature gradient forms across the films. Fig. S11 illustrates the measurement of the temperature

gradients. The top surface of the films is immersed in air or electrolyte for easy thermal transport and will effectively cool. However, the film's bottom is not conducive to thermal transport due to the glass's relatively poor thermal conductivity and will stay warm. Indeed, significant temperature gradients were observed under one-sun illumination in the air for the three films, as shown in Fig. 3b. The composite film showed a maximum temperature gradient of around 29 °C, which is 4 °C and 10 °C larger than bare NCO and CBO film, respectively. The temperature gradients were also collected during PEC operation. As shown in Fig. 3c, the temperature gradients of NCO and NCO/CBO films are very close, with a maximum value of around 22 °C, while the CBO gradient only reaches 14 °C. It should be noted that measured temperature gradients are expected to be lower than the actual values since the temperature at the interface of the NCO layer and the glass substrate is difficult to measure during cell operation.

As mentioned in the introduction, NCO is a well-studied thermo-electric material, which can generate a voltage difference across a thermal gradient through the Seebeck effect [39]. Our NCO layer has a Seebeck coefficient around 150–200 V K^{-1} (Fig. 3d) and a conductivity of 71.4 S cm^{-1} (Fig. S12, $\sigma = 1/\rho$). These values agree well with those found in previous reports [40] and establish the thermoelectric capa-bility of our NCO layer. Combining the above results, photocurrent at 0.45 V *vs*. RHE under increasing temperature gradients for each photo-electrode material (summarizing results from Fig. 2a–c and Fig. 3c). The
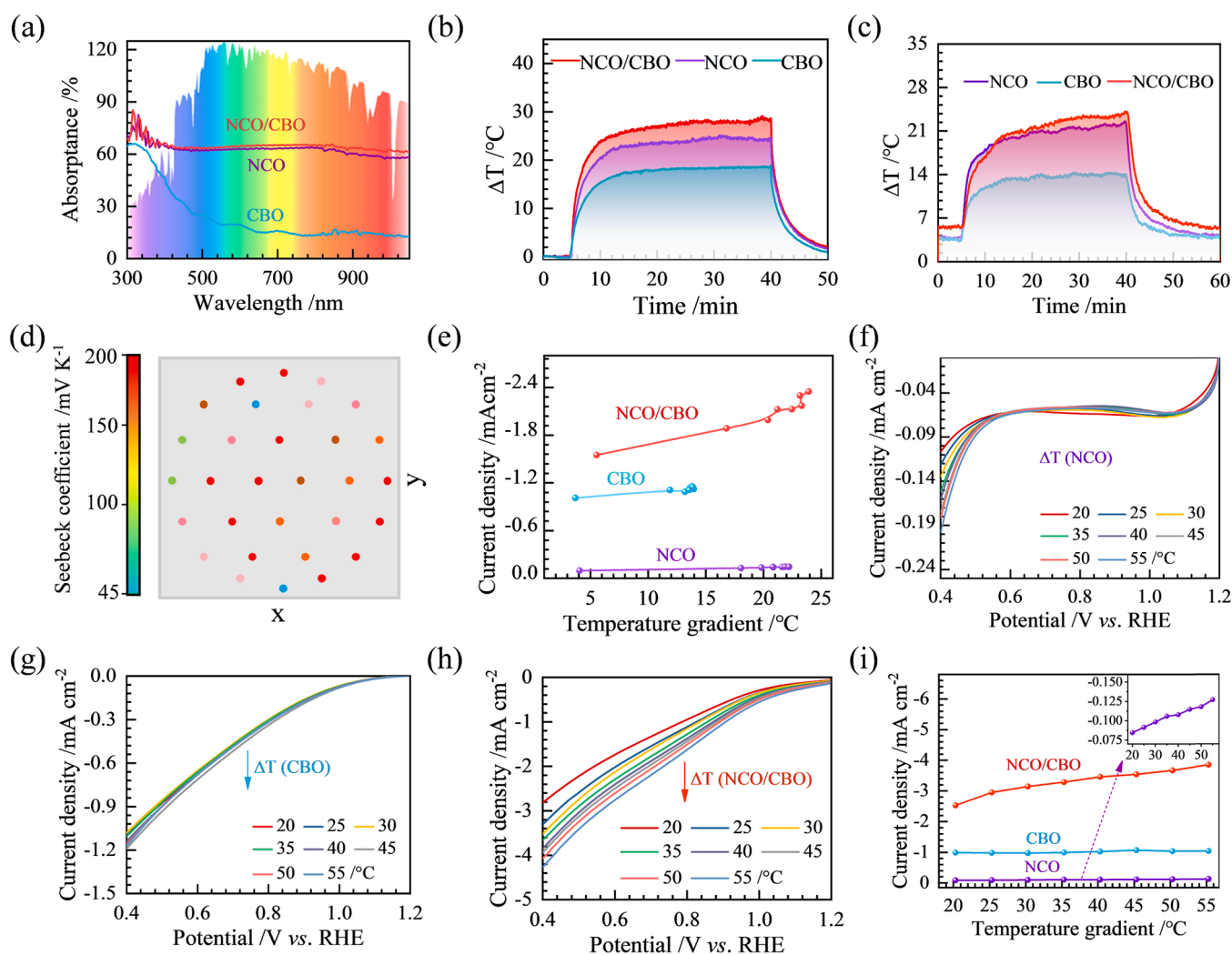

Fig. 3. The UV–vis absorption spectra of NCO, CBO, and NCO/CBO films (a). the temperature gradients of the three films under one-sun illumination in the air (b) and PEC cell (c). The Seebeck coefficient map of the NCO film (d). Photocurrent (e) at 0.45 V *vs*. RHE under different temperature gradients. The *J-V* curves of NCO (f), CBO (g), NCO/CBO (h), and the corresponding photocurrent (i) at 0.45 V *vs*. RHE under different temperature gradients.

performance of bare CBO film was barely improved. In comparison, NCO/CBO films show significant photocurrent enhancement as the temperature gradient increases. The photocurrent of NCO/CBO film increased from -1.9 to -2.8 mA cm^{-2} as the temperature gradient raised from 16.7 to 23.9 °C. We conclude that introducing the NCO layer enhances the light-harvesting capacity of the composite films, contributing to the conversion of absorbed photons to heat via the photothermal effect. Thus, a thermal gradient is generated, and the NCO layer produces a voltage difference across this thermal gradient via the thermoelectric effect, ultimately improving the performance of the photoelectrode.

To further confirm the synergistic effect of photothermoelectricity and photoelectricity, photocurrent was investigated as a function of controlled temperature gradients, where illumination time was not involved. Fig. S13 shows a schematic illustration of the homemade temperature-controlled PEC cell used herein. The ceramic heating plate was fixed on the back of the samples as the hot point, and the front side of the samples was immersed in the electrolyte to keep at a constant temperature as the cool point. A micro patch temperature sensor and precision temperature controller can precisely control the temperature gradient between hot and cool points. The *J-V* curves in Fig. 3f–h and the corresponding photocurrent at 0.45 V *vs*. RHE in Fig. 3i shows that the

PEC performance of NCO and NCO/CBO films significantly increased as the temperature gradient was raised from 20 °C to 55 °C. The corresponding J-V curves under dark are shown in Fig. S14. The maximum photocurrent of the composite photocathode reached about -4 mA cm^{-2} at 0.45 V *vs*. RHE, which is among the highest reported values for CBO-based photocathodes [41]. As expected, the performance improvement of bare CBO was negligible (only ~ 0.02 mA cm^{-2}). These results further confirmed the synergy of photothermoelectricity and photoelectricity, which deserves the greatest attention. Moreover, the J-V responses of NCO, CBO, and NCO/CBO photocathodes under different electrolyte temperatures (Fig. S15) were measured to show the weak effect of reactive temperature.

3.4. Thermoelectric enhanced carrier dynamics

Improved carrier dynamics are the essential reason for the enhanced performance of the composite film. To better understand it, charge separation efficiency (η_{sep}) was calculated by the following equation: $J_{sacr} = J_{abs} \times \eta_{sep}$, where J_{abs} is the theoretical maximum photocurrent of photoelectrodes under one-sun illumination, and J_{sacr} is the measured photocurrent in the presence of an electron sacrificial agent [41,42]. According to Fig. 4a and b, as the temperature gradient increased, the
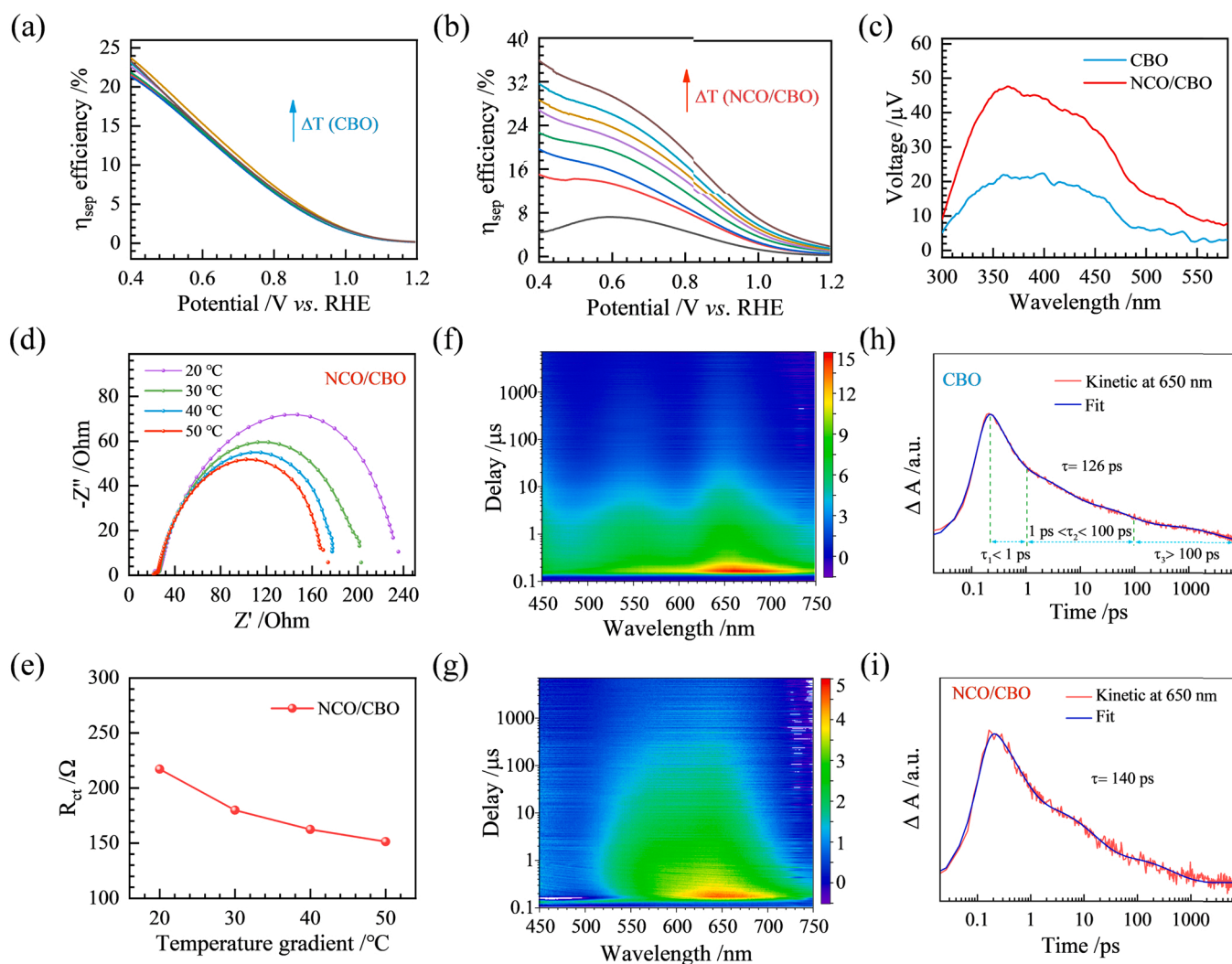

Fig. 4. The charge separation efficiency of CBO (a) and NCO/CBO (b) films. The SPV spectra of CBO and NCO/CBO films (c). The PEIS (d) and Bode (e) plots of NCO/CBO under controlled temperature gradients. Transient absorption contour maps of CBO (f) and NCO/CBO (g) films in the range of -100 fs to 7.4 ns. Excitation wavelength: 320 nm, power: 0.8 μJ per pulse, beam diameter: 0.3 mm. Time dependence of dA signals and related fitting curves for CBO (h) and NCO/CBO (i) at 650 nm probe wavelength.

separation efficiency of pure CBO did not appreciably change. However, that of NCO/CBO remarkably improved from ~ 8 to 36%. Such an enhancement in η_{sep} can also be seen in the long-time one-sun illumination experiment (Fig. S16), indicating that the presence of NCO significantly improved the separation of photogenerated carriers. This result is further confirmed by the surface photovoltage spectrum (SPS), which offers unique advantages in investigating the separation and transport of photogenerated charge carriers, both in the surface and bulk of semiconductor materials [43]. The positive surface photovoltage (SPV) in Fig. 4c means that the photogenerated electrons move to the bright side of the film and separate with holes. The strong SPV peak appearing in the range of 300–600 nm is consistent with the absorption peak of CBO in the UV–vis spectrum. After 10 min illumination, the SPV signal of the composite film increased. This result further confirmed that the thermoelectric potential as the driving force could promote the separation of photogenerated carriers in the bulk of NCO/CBO films. Additionally, the synergistic effect not only enhances the charge separation efficiency but also improves the charge transport in the films. Nyquist plots and the fitted R_{ct} in Fig. 4d,e show that the charge transfer resistance of the NCO/CBO film decreased continuously as the temperature gradient increased. Compared with the constant charge transfer resistance of the CBO film (Fig. S17), the reduced resistance for the NCO/CBO film is another advantage of the synergy of the photoelectricity and the photothermoelectricity.

Carrier lifetime is another key parameter of charge carrier dynamics and was investigated using transient absorption spectroscopy [44]. Fig. 4f shows the absorption contour map of bare CBO that contains two main peaks located at 550 nm and 650 nm, which decrease over time. These peaks are attributed to the ligand-to-metal charge transition between O-to-Bi (2.27 eV) and O-to-Cu (1.82 eV), respectively [25,45]. Due to the increased thickness and decreased peak intensity of the NCO/CBO film, the two peaks combine into one broad peak in Fig. 4g. Fig. 4h and i are the absorption spectra extracted from the contour maps of bare CBO and NCO/CBO films in the visible region at different delay times. The sharpness of signals from thin-film semiconductors is related to a modification of the semiconductor's optical properties (the complex index of refraction) due to the perturbation of the charge carrier band population by the pump pulse. This contrasts with the perspective utilized in molecular spectroscopy, where the positive signals are attributed to nonequilibrium populations of excited states generated by the pump pulse (photo-induced absorption), and the negative signs are associated with depopulation of the ground states (bleach) [46]. Fig. 4h and i show the carrier dynamics of bare CBO and NCO/CBO films extracted from the absorption spectra. The kinetic traces at 650 nm with 400 nm excitation were well fitted via Eq. (2):

$$\Delta A(t) = k_1 e^{-t/\tau 1} + k_2 e^{-t/\tau 2} + k_3 e^{-t/\tau 3} \quad (2)$$

Where τ_1, τ_2, and τ_3 are time constants, and k_1, k_2, and k_3 are weightings (amplitudes). The first time constant (τ_1) is related to hot carrier cooling through carrier-carrier scattering and momentum relaxation, commonly less than 1 ps. The second time constant (τ_2) is associated with energy relaxation involving carrier-phonon scattering. The third time constant (τ_3) is attributed to the trap and recombination of charge carriers [24, 47–49]. The final carrier lifetime was calculated by summing these 3-time constants with weights. The NCO/CBO shows an 11% enhancement in carrier lifetime over that of bare CBO. We attribute this improvement to the laser-induced heating effect and the resultant thermoelectric potential of the NCO bottom layer. Typically, part of the pump light energy converts to thermal energy through the photothermal effect, and the consequent temperature gradient across the NCO layer causes a thermoelectric potential. As an internal electric field, it improves bulk charge separation inside the semiconductor films and increases charge carrier lifetime.

3.5. Simulation and mechanism schematic

To gain more insight into the mechanism of the NCO/CBO composite photoelectrode, the process was simulated using COMSOL Multiphysics software. The thermoelectric property of NCO and its influence on the CBO layer under different temperature gradients were studied. As shown in Fig. 5a and Fig. S18, when a temperature gradient of 50 °C was applied between the bottom and top of the NCO layer, a thermoelectric voltage of 0.01 V was generated with high potential at the top of the NCO. The thermoelectric voltage influenced the distribution of charge carriers in the CBO film. Fig. 5b,c display that the electrons or holes are preferably located at the top or bottom of the film, respectively. By contrast, carriers are uniformly distributed as the temperature gradient goes zero without thermoelectric voltage (Fig. S19,20). Such spatially separated distribution is beneficial for charge collections by inhibiting carrier recombination. These results confirm that the NCO layer performs a thermoelectric function, converting temperature gradient to thermoelectric potential and creating an internal electric field to promote the separation and migration of charge carriers.

Fig. 5d displays a schematic diagram of charge transport in the NCO/CBO composite photoelectrode. Due to the photothermal effect, a temperature gradient is formed between the top and bottom of the film under sunlight illumination, with the top side relatively cooler than the bottom. Because NCO is p-type thermoelectric material, the majority carrier (holes) diffuse to the cool side [50]. Therefore, the cool side becomes enriched with holes, and the hot side gathers electrons. As a result, a thermoelectric potential is formed, with high and low potential represented by "+" and "−", respectively. In the meantime, the FTO substrate shows the same low potential as the hot side of NCO due to the direct connection. As for the CBO, the photogenerated electrons and holes are effectively separated in the space charge region. Electrons migrate to the surface and participate in the redox reaction. At the same time, holes diffuse into the field-free region and are collected by the FTO substrate under the driving force from the thermoelectric potential. Consequently, the internal thermoelectric potential facilitates charge separation and decreases the recombination probability, resulting in significantly enhanced PEC performance.

4. Conclusion

In summary, a novel photoelectrode was designed and fabricated to integrate the thermoelectric effect into CBO-based photoelectrodes to boost the solar-to-H_2O_2 PEC conversion efficiency. *J-V* responses clearly showed that the integrated NCO thermoelectric layer significantly improved the photocurrent by 64% during sunlight illumination. Operando thermo-controlled measurements revealed that the temperature gradient considerably modulated the performance of composite films. The maximum photocurrent of the composite photocathode of about − 4 mA cm^{-2} at 0.45 V *vs*. RHE appeared at a temperature gradient of 55 °C, which is among the best-reported values for CBO-based photocathodes. Moreover, the NCO/CBO composite displayed highly efficient H_2O_2 production at a concentration of 192.9 μmol/L with an applied bias at 0.4 V *vs*. RHE, which is about 2.4 times faster than that of pure CBO. Also, NCO/CBO exhibited a favorable FE of 47.42%. In-situ charge separation, surface photovoltage, and PEIS measurements revealed that such performance enhancement is primarily due to improved charge collection. The bottom NCO thermoelectric layer produces electricity from the temperature gradient to drive the separation and transfer of photogenerated charge carriers in the bulk of the CBO. Extended carrier lifetime from transient absorption spectroscopy further confirmed effective charge separation in bulk. COMSOL Multiphysics simulations displayed an internal electric field and its beneficial modulation on the spatial distribution of charges. More broadly, this work demonstrates the successful integration of thermoelectricity with photochemistry to optimize photoelectrodes in practical applications like solar-to-H_2O_2 conversion.
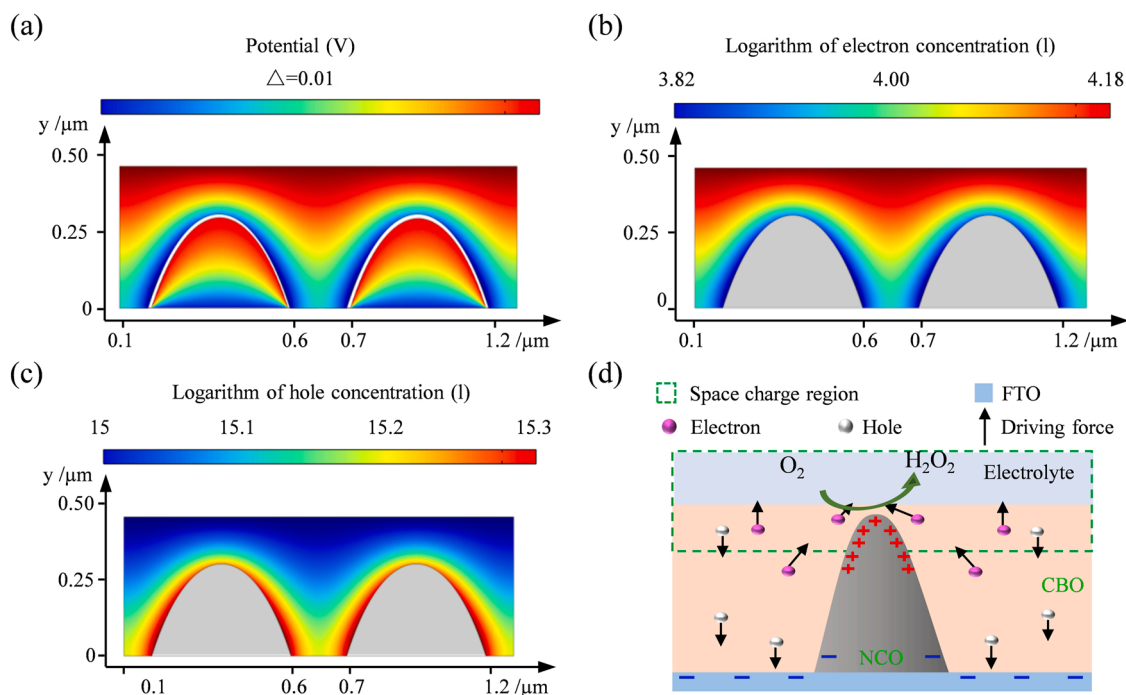
Fig. 5. The influence of thermoelectric effect on the potential (a) and the carrier distribution in the CBO layer (b, c) calculated by COMSOL. For NCO, $\Delta T = 50\ ^{\circ}C$ and Seebeck coefficient $\neq 0$A schematic illustration of charge transport in the NCO/CBO composite (d).

Authorship contribution statement

Mengdi Sun and Zemin Zhang carried out the whole experiments and wrote the paper. Bo Liu carried out the COMSOL simulation. Weihua Han revised the manuscript. Zemin Zhang and Mingzheng Xie supervised the research and revised the manuscript.

CRediT authorship contribution statement

Mengdi Sun: Data curation, Writing – original draft, Methodology. **Bo Liu:** Simulation. **Weihua Han:** Reviewing. **Zemin Zhang:** Supervision, Writing – review & editing. **Mingzheng Xie:** Supervision, Writing – review & editing.

Declaration of Competing Interest

The authors declare that they have no known competing financial interests or personal relationships that could have appeared to influence the work reported in this paper.

Acknowledgment

Appendix A. Supporting information

Supplementary data associated with this article can be found in the online version at doi:10.1016/j.apcatb.2021.120980.

References

[1] X. Chen, W. Zhang, L. Zhang, L. Feng, C. Zhang, J. Jiang, T. Yan, H. Wang, Sacrificial agent-free photocatalytic H$_2$O$_2$ evolution via two-electron oxygen reduction using a ternary α-Fe$_2$O$_3$/CQD@g-C$_3$N$_4$ photocatalyst with broad-spectrum response, J. Mater. Chem. A 8 (2020) 18816–18825.

[2] Z. Li, Q. Xu, F. Gou, B. He, W. Chen, W. Zheng, X. Jiang, K. Chen, C. Qi, D. Ma, Orthogonal modular biosynthesis of nanoscale conjugate vaccines for vaccination against infection, Nano Res. (2021) 1–9.

[3] K. Mase, M. Yoneda, Y. Yamada, S. Fukuzumi, Seawater usable for production and consumption of hydrogen peroxide as a solar fuel, Nat. Commun. 7 (2016) 11470.

[4] T.M. Gill, L. Vallez, X. Zheng, The role of bicarbonate-based electrolytes in H$_2$O$_2$ production through two-electron water oxidation, ACS Energy Lett. 6 (2021) 2854–2862.

[5] T.H. Jeon, H. Kim, H.-i Kim, W. Choi, Highly durable photoelectrochemical H$_2$O$_2$ productionviadual photoanode and cathode processes under solar simulating and external bias-free conditions, Energy Environ. Sci. 13 (2020) 1730–1742.

[6] Z. Teng, W. Cai, W. Sim, Q. Zhang, C. Wang, C. Su, T. Ohno, Photoexcited single metal atom catalysts for heterogeneous photocatalytic H$_2$O$_2$ production: pragmatic guidelines for predicting charge separation, Appl. Catal. B: Environ. 282 (2021), 119589.

[7] Y. Jiang, P. Ni, C. Chen, Y. Lu, P. Yang, B. Kong, A. Fisher, X. Wang, Selective electrochemical H$_2$O$_2$ production through two-electron oxygen electrochemistry, Adv. Energy Mater. 8 (2018) 1801909.

[8] Y. Chen, X. Feng, Y. Liu, X. Guan, C. Burda, L. Guo, Metal oxide-based tandem cells for self-biased photoelectrochemical water splitting, ACS Energy Lett. 5 (2020) 844–866.

[9] S. Wang, G. Liu, L. Wang, Crystal facet engineering of photoelectrodes for photoelectrochemical water splitting, Chem. Rev. 119 (2019) 5192–5247.

[10] R. Gottesman, I. Levine, M. Schleuning, R. Irani, D. Abou-Ras, T. Dittrich, D. Friedrich, R. Krol, Overcoming phase-purity challenges in complex metal oxide photoelectrodes: a case study of CuBi$_2$O$_4$, Adv. Energy Mater. 11 (2021) 2003474.

[11] Y. Natanzon, A. Azulay, Y. Amouyal, Evaluation of polaron transport in solids from first-principles, Isr. J. Chem. 60 (2020) 768–786.

[12] A.J. Rettie, W.D. Chemelewski, D. Emin, C.B. Mullins, Unravelling small-polaron transport in metal oxide photoelectrodes, J. Phys. Chem. Lett. 7 (2016) 471–479.

[13] G. Segev, C.-M. Jiang, J.K. Cooper, J. Eichhorn, F.M. Toma, I.D. Sharp, Quantification of the loss mechanisms in emerging water splitting photoanodes through empirical extraction of the spatial charge collection efficiency, Energy Environ. Sci. 11 (2018) 904–913.

[14] Z. Zhao, H. Zhou, L. Zheng, P. Niu, G. Yang, W. Hu, J. Ran, S. Qiao, J. Wang, H. Zheng, Molecules interface engineering derived external electric field for effective charge separation in photoelectrocatalysis, Nano Energy 42 (2017) 90–97.

[15] J. Li, L. Cai, J. Shang, Y. Yu, L. Zhang, Giant enhancement of internal electric field boosting bulk charge separation for photocatalysis, Adv. Mater. 28 (2016) 4059–4064.

[16] W. Zhang, D. Yan, X. Tong, M. Liu, Ultrathin lutetium oxide film as an epitaxial hole-blocking layer for crystalline bismuth vanadate water splitting photoanodes, Adv. Funct. Mater. 28 (2018) 1705512.

[17] Q. Chen, X. Chen, Q. Jiang, Z. Zheng, Z. Song, Z. Zhao, Z. Xie, Q. Kuang, Constructing oxide/sulfide in-plane heterojunctions with enlarged internal electric

field for efficient CO$_2$ photoreduction, Appl. Catal. B: Environ. 297 (2021), 120394.

[18] J. Fu, K. Jiang, X. Qiu, J. Yu, M. Liu, Product selectivity of photocatalytic CO$_2$ reduction reactions, Mater. Today 32 (2020) 222–243.

[19] Y. Guo, W. Shi, Y. Zhu, Internal electric field engineering for steering photogenerated charge separation and enhancing photoactivity, EcoMat 1 (2019).

[20] D. Xiang, Z. Liu, M. Wu, H. Liu, X. Zhang, Z. Wang, Z.L. Wang, L. Li, Enhanced piezo-photoelectric catalysis with oriented carrier migration in asymmetric Au-ZnO nanorod array, Small 16 (2020), e1907603.

[21] J. Song, T.L. Kim, J. Lee, S.Y. Cho, J. Cha, S.Y. Jeong, H. An, W.S. Kim, Y.-S. Jung, J. Park, G.Y. Jung, D.-Y. Kim, J.Y. Jo, S.D. Bu, H.W. Jang, S. Lee, Domain-engineered BiFeO$_3$ thin-film photoanodes for highly enhanced ferroelectric solar water splitting, Nano Res. 11 (2017) 642–655.

[22] H. Li, Y. Yu, M.B. Starr, Z. Li, X. Wang, Piezotronic-enhanced photoelectrochemical reactions in Ni(OH)$_2$-decorated ZnO photoanodes, J. Phys. Chem. Lett. 6 (2015) 3410–3416.

[23] H. He, C. Zhang, T. Liu, Y. Cao, N. Wang, Z. Guo, Thermoelectric–photoelectric composite nanocables induced a larger efficiency in dye-sensitized solar cells, J. Mater. Chem. A 4 (2016) 9362–9369.

[24] Y. Dou, F. Wu, L. Fang, G. Liu, C. Mao, K. Wan, M. Zhou, Enhanced performance of dye-sensitized solar cell using Bi$_2$Te$_3$ nanotube/ZnO nanoparticle composite photoanode by the synergistic effect of photovoltaic and thermoelectric conversion, J. Power Sources 307 (2016) 181–189.

[25] J.K. Cooper, Z. Zhang, S. Roychoudhury, C.-M. Jiang, S. Gul, Y.-S. Liu, R. Dhall, A. Ceballos, J. Yano, D. Prendergast, S.E. Reyes-Lillo, CuBi$_2$O$_4$: electronic structure, optical properties, and photoelectrochemical performance limitations of the photocathode, Chem. Mater. 33 (2021) 934–945.

[26] F. Wang, W. Septina, A. Chemseddine, F.F. Abdi, D. Friedrich, P. Bogdanoff, R. van de Krol, S.D. Tilley, S.P. Berglund, Gradient self-doped CuBi$_2$O$_4$ with highly improved charge separation efficiency, J. Am. Chem. Soc. 139 (2017) 15094–15103.

[27] R. Gottesman, A. Song, I. Levine, M. Krause, A.T.M.N. Islam, D. Abou-Ras, T. Dittrich, R. Krol, A. Chemseddine, Pure CuBi$_2$O$_4$ photoelectrodes with increased stability by rapid thermal processing of Bi$_2$O$_3$/CuO grown by pulsed laser deposition, Adv. Funct. Mater. 30 (2020) 1910832.

[28] J. Zhang, G. Zhang, Q. Ji, H. Lan, J. Qu, H. Liu, Carbon nanodot-modified FeOCl for photo-assisted Fenton reaction featuring synergistic in-situ H$_2$O$_2$ production and activation, Appl. Catal. B: Environ. 266 (2020), 118665.

[29] N.K. Veldurthi, N.K. Eswar, S.A. Singh, G. Madras, Cocatalyst free Z-schematic enhanced H$_2$ evolution over LaVO$_4$/BiVO$_4$ composite photocatalyst using Ag as an electron mediator, Appl. Catal. B: Environ. 220 (2018) 512–523.

[30] X. Zhang, C. Li, J. Liang, J. Wang, J. Zhang, X. Chen, F. Wang, R. Li, Selective routing of spatial information flow from input to output in hippocampal granule cells, ChemCatChem 12 (2020) 1212–1219.

[31] Z. Zhang, S.A. Lindley, R. Dhall, K. Bustillo, W. Han, E. Xie, J.K. Cooper, Beneficial CuO phase segregation in the ternary p-type oxide photocathode CuBi$_2$O$_4$, ACS Appl. Energy Mater. 2 (2019) 4111–4117.

[32] S. Maensiri, W. Nuansing, Thermoelectric oxide NaCo$_2$O$_4$ nanofibers fabricated by electrospinning, Mater. Chem. Phys. 99 (2006) 104–108.

[33] Z. Zhang, S.A. Lindley, D. Guevarra, K. Kan, A. Shinde, J.M. Gregoire, W. Han, E. Xie, J.A. Haber, J.K. Cooper, Fermi level engineering of passivation and electron transport materials for p-Type CuBi$_2$O$_4$ employing a high-throughput methodology, Adv. Funct. Mater. 30 (2020) 2000948.

[34] J. Lee, H. Yoon, K.S. Choi, S. Kim, S. Seo, J. Song, B.U. Choi, J. Ryu, S. Ryu, J. Oh, C. Jeon, S. Lee, Template engineering of CuBi$_2$O$_4$ single-crystal thin film photocathodes, Small 16 (2020), e2002429.

[35] L. Chen, L. Wang, Y. Wan, Y. Zhang, Z. Qi, X. Wu, H. Xu, Acetylene and diacetylene functionalized covalent triazine frameworks as metal-free photocatalysts for hydrogen peroxide production: a new two-electron water oxidation pathway, Adv. Mater. 32 (2020), e1904433.

[36] F. Ye, T. Wang, X. Quan, H. Yu, S. Chen, Constructing efficient WO$_3$-FPC system for photoelectrochemical H$_2$O$_2$ production and organic pollutants degradation, Chem. Eng. J. 389 (2020), 123427.

[37] T. Liu, X. Zhang, F. Zhao, Y. Wang, Targeting inside charge carriers transfer of photocatalyst: selective deposition of Ag$_2$O on BiVO$_4$ with enhanced UV–vis–NIR photocatalytic oxidation activity, Appl. Catal. B: Environ. 251 (2019) 220–228.

[38] Y. Xu, J. Jian, F. Li, W. Liu, L. Jia, H. Wang, Porous CuBi$_2$O$_4$ photocathodes with rationally engineered morphology and composition towards high-efficiency photoelectrochemical performance, J. Mater. Chem. A 7 (2019) 21997–22004.

[39] T. Liu, C. Wang, J. Hou, C. Zhang, H. Chen, H. He, N. Wang, H. Wu, G. Cao, Enhanced electron collection in perovskite solar cells employing thermoelectric NaCo$_2$O$_4$/TiO$_2$ coaxial nanofibers, Small 12 (2016) 5146–5152.

[40] K. Park, K.U. Jang, H.C. Kwon, J.G. Kim, W.S. Cho, Antigenic determinants to GAD autoantibodies in patients with type 1 diabetes with and without autoimmune thyroid disease, J. Alloy. Compd. 419 (2006) 213–219.

[41] F.F. Abdi, L. Han, A.H. Smets, M. Zeman, B. Dam, R. van de Krol, Efficient solar water splitting by enhanced charge separation in a bismuth vanadate-silicon tandem photoelectrode, Nat. Commun. 4 (2013) 2195.

[42] Z. Zhang, Y. Li, X. Jiang, W. Han, M. Xie, F. Wang, E. Xie, Significantly improved charge collection and interface injection in 3D BiVO$_4$ based multilayered core-shell nanowire photocatalysts, Nanoscale 9 (2017) 14015–14022.

[43] Y. Yang, F. Teng, Y. Kan, L. Yang, Z. Liu, W. Gu, A. Zhang, W. Hao, Y. Teng, Biological phosphorus removal in an extended ASM2 model: Roles of extracellular polymeric substances and kinetic modeling, Appl. Catal. B: Environ. 205 (2017) 412–420.

[44] A. Kafizas, X. Wang, S.R. Pendlebury, P. Barnes, M. Ling, C. Sotelo-Vazquez, R. Quesada-Cabrera, C. Li, I.P. Parkin, J.R. Durrant, Where do photogenerated holes go in anatase:rutile TiO$_2$? A transient absorption spectroscopy study of charge transfer and lifetime, J. Phys. Chem. A 120 (2016) 715–723.

[45] Z. Zhang, S.A. Lindley, D. Guevarra, K. Kan, A. Shinde, J.M. Gregoire, W. Han, E. Xie, J.A. Haber, J.K. Cooper, Fermi level engineering of passivation and electron transport materials for p-Type CuBi$_2$O$_4$ employing a high-throughput methodology, Adv. Funct. Mater. 30 (2020) 2000948.

[46] S. Liu, J. Chen, D. Liu, L. Shan, X. Zhang, Dispersibility and characterization of polyvinyl alcohol–coated magnetic nanoparticles in poly(glycerol sebacate) for biomedical applications, J. Nanopart. Res. 21 (2019) 275.

[47] L. Shenje, S. Larson, Y. Zhao, S. Ullrich, Composition effects on ultrafast optical properties of Cu$_x$O$_y$ thin films: a transient absorption study, J. Phys. Chem. C 124 (2020) 24908–24918.

[48] B. Born, J.D.A. Krupa, S. Geoffroy-Gagnon, I.R. Hristovski, C.M. Collier, J. F. Holzman, Ultrafast charge-carrier dynamics of copper oxide nanocrystals, ACS Photonics 3 (2016) 2475–2481.

[49] M. Li, J. Fu, Q. Xu, T.C. Sum, Slow hot-carrier cooling in halide perovskites: prospects for hot-carrier solar cells, Adv. Mater. 31 (2019), e1802486.

[50] S.N. Guin, K. Biswas, Sb deficiencies control hole transport and boost the thermoelectric performance of p-type AgSbSe$_2$, J. Mater. Chem. C 3 (2015) 10415–10421.